ACS SENSORS

pubs.acs.org/acssensors
Article

Deep Learning-driven Microfluidic-SERS to Characterize the Heterogeneity in Exosomes for Classifying Non-Small Cell Lung Cancer Subtypes

Hui Chen,* Hongyi Liu, Longqiang Xing, Dandan Fan, Nan Chen, Pei Ma, and Xuedian Zhang

Cite This: ACS Sens. 2025, 10, 2872–2882
Read Online

ABSTRACT: Lung cancer exhibits strong heterogeneity, and its early diagnosis and precise subtyping are of great importance, as they can increase the ability to deliver personalized medicines by tailoring therapy regimens. Tissue biopsy, albeit the gold standard, is invasive, costly and provides limited information about the tumor and its molecular landscape. Exosomes, as promising biomarkers for lung cancer, are a heterogeneous collection of membranous vesicles containing tumor-specific information for liquid biopsy to identify lung cancer subtypes. However, the small size, complex structure, and heterogeneous molecular features of exosomes pose significant challenges for their effective isolation and analysis. Herein, we report a deep learning-driven microfluidic chip with surface-enhanced Raman scattering (SERS) readout to characterize the differences in exosomes for the early diagnosis and molecular subtyping of non-small cell lung cancer (NSCLC). This integration comprises a processing unit for exosome capture and enrichment using polystyrene microspheres (PS) binding gold nanocubes (AuNCs) and anti-CD-9 antibody (denoted as PACD), and an optical sensing unit to trap the PACD and detect SERS signals from these exosomes. This system achieved a maximum trapping efficiency of 85%, and could distinguish three different NSCLC cell lines from the normal cell line with an overall accuracy of 97.88% and an area under the curve (AUC) of over 0.95 for each category. This work highlights the combined power of deep learning, SERS, and microfluidics in realizing the capture, detection, and analysis of exosomes from biological matrices, which may pave the way for clinical exosome-based cancer diagnosis and prognostication in the future.

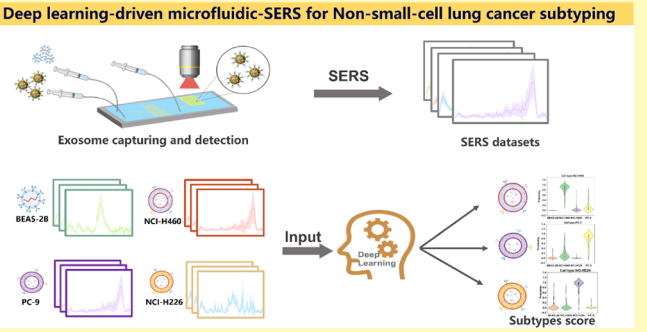

KEYWORDS: *exosome, lung cancer, surface-enhanced raman scattering, microfluidic, deep learning*

Lung cancer, accounting for 14% of all new cancer cases and a quarter of cancer deaths globally, is categorized into non-small cell lung cancer (NSCLC, 85%) and small cell lung cancer (SCLC, 15%) based on histological and origin differences.[1] The subtypes of NSCLC primarily consist of lung adenocarcinoma (LUAD), lung squamous cell carcinoma (LUSC), and large cell lung cancer (LCC). Among these, the first two are the predominant subtypes, while LCC is relatively rare.[2] Regrettably, due to the lack of effective early diagnostic strategies, up to 70% of lung cancer patients are diagnosed at an advanced stage, with a five-year survival rate of only 16% to 18%.[3] Apart from the challenge of early diagnosis, NSCLC subtyping is also crucial, as there are significant differences in biological characteristics, treatment response, and prognosis among different subtypes of lung cancer.[4,5] Currently, clinical techniques for NSCLC diagnosis mainly consist of computed tomography (CT), magnetic resonance imaging (MRI), bronchoscopy, and a transthoracic needle aspiration biopsy. Despite their widespread use, these methods have limitations, such as restricted detection capabilities and potential irreversible physical harm to patients.[6] Hence, exploring a noninvasive and accurate detection method is urgent. Liquid biopsy has emerged against this backdrop, bringing new ideas for early NSCLC diagnosis and subtyping. It only requires the collection of trace body fluids from patients, including sweat, saliva, urine, and serum, enabling the acquisition of tumor-related information and demonstrating significant application potential.[7,8]

Exosomes, as a novel and highly promising biomarker in the field of liquid biopsy, have been demonstrated to play a significant role in the occurrence, development, diagnosis, and treatment of disease.[9] They are extracellular vesicles with a size ranging from 30 to 200 nm, secreted by cells into the surrounding biofluids, including cancer cells. Exosomes have a

Received: December 18, 2024
Revised: March 5, 2025
Accepted: March 27, 2025
Published: April 1, 2025

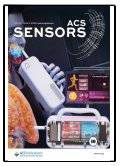

https://doi.org/10.1021/acssensors.4c03621
ACS Sens. 2025, 10, 2872−2882

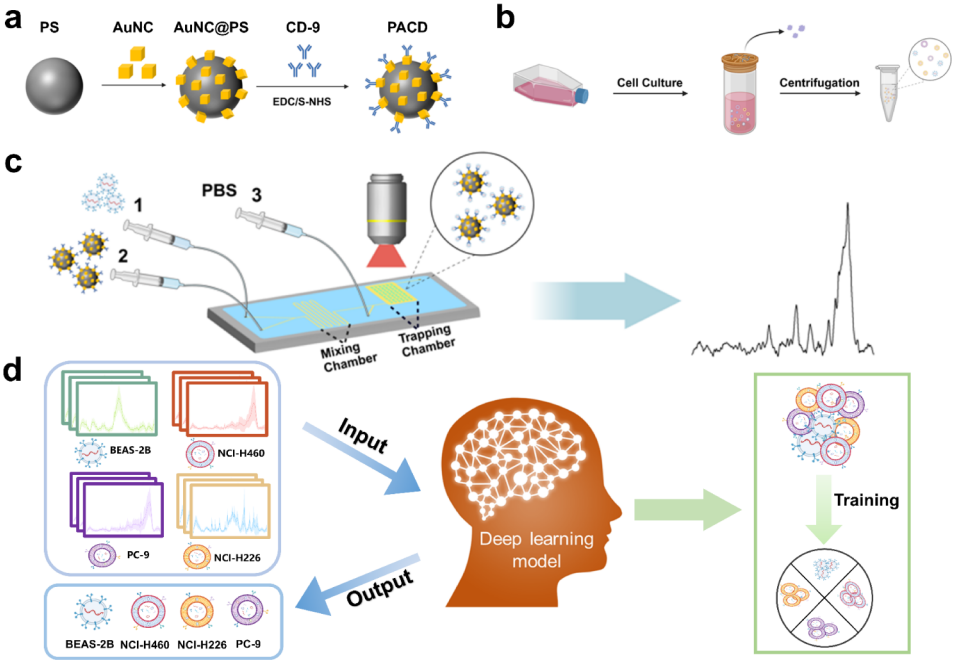

Figure 1. Schematic illustration of a microfluidic platform integrated with label-free SERS and deep learning to characterize exosomes for the subtyping of NSCLC. (a) The synthesis of the exosome capture probe PACD. (b) Extraction of exosomes. (c) Microfluidic-SERS Chip for exosome capture and SERS detection. (d) Overview of deep learning-based classification of NSCLC exosomes using SERS signal patterns.

lipid bilayer structure that encloses a rich collection of tumor-related biomolecules, including nucleic acids, proteins, lipids, and metabolites.[10] These exosomal molecules provide clues to their origin, rendering exosomes strongly heterogeneous.[11] If the heterogeneity in exosomes from lung cancer can be fully characterized, then distinguishing NSCLC subtypes would be a possibility. However, heterogeneity can be a double-edged sword. The natural heterogeneity of exosomes in terms of size, function, and molecular features poses significant obstacles for efficient capture and precise analysis.[12]

Recently, the microfluidic technique has drawn significant attention as a potential tool to address the challenges associated with the capture and detection of exosomes. Capable of handling samples at microscale to nanoscale levels, microfluidics can offer automated processes with high precision while requiring only a minimal volume. In addition, it allows detection techniques to be integrated into a single unit.[13] Various detection methods, including fluorescence detection,[14] colorimetry,[15] electrochemical,[16] nuclear magnetic resonance (NMR),[17] and surface-enhanced Raman scattering (SERS),[18] have been employed for the detection of exosomes. Among these, SERS has gained particular attention due to its high sensitivity and fingerprint characteristics.[19] Its advantages are mainly manifested in the following aspects: it offers molecular-leveled structural information on analytes by enhancing Raman signals through noble metal nanostructures; as a noninvasive and nondestructive technology, SERS enables highly sensitive detection; at the same time, it is less interfered by water and can construct real-time analysis.[20] Thus, microfluidic devices integrated with SERS spectroscopy enable easy and precise manipulation of samples as well as rapid and sensitive readout.[21] Currently, the combination of SERS and microfluidic technology for exosome detection mainly utilizes a labeled approach with specific Raman reporters. Consequently, only very limited proteins or nucleic acid molecules can be identified in exosomes, which inevitably ignores much useful information related to cancer.[22] In contrast, label-free SERS eliminates the need for additional labeling steps, directly analyzing the Raman signals of the analyte itself, providing a more comprehensive view of the analyte, and avoiding issues of nonspecific interference and background signals caused by labels.[23] In view of this, microfluidic technology with label-free SERS readout is able to simplify the detection process while providing a comprehensive molecular pattern of exosomes without the need to target specific markers.

Given the complex molecular composition of exosomes, deep learning technology can be utilized to address the complexity and heterogeneity of label-free spectral data from exosomes.[24,25] Deep learning is capable of extracting hidden, effective, and comprehensible information from complex SERS data, thereby enabling precise identification and classification of target molecular features.[26,27] Cao et al. developed a PCA-TLNN-based SERS analysis platform for the identification of gastric cancer, achieving an impressive accuracy of 97.5%.[28] Our previous work employed a deep learning algorithm to analyze SERS spectra of kidney recipients' urine samples for the diagnosis of kidney allograft injury, achieving an accuracy of 93.03%.[29] However, it is notable that deep learning models learn optimized features through multilayered neural networks. These networks consist of complex, nonlinear interactions between layers, making it difficult to trace how input data are transformed into final decisions. This inherent opacity has led to deep learning being widely described as a black box, which raises serious concerns. Particularly in medical applications, this lack of transparency can have life-critical consequences. Currently, very few studies report deep learning with explanation functions for SERS spectral data processing. If explainable deep learning were applied to SERS data to reflect logical decision-making information, it could bridge the gap between model performance and human-understandable explanations of AI-driven decisions. Thus, pairing the microfluidic platform with label-free SERS readout and deep learning

https://doi.org/10.1021/acssensors.4c03621
ACS Sens. 2025, 10, 2872−2882

will bring new inspiration to the capture, detection, and analysis of exosomes.

Herein, we propose a microfluidic platform integrated with label-free SERS and deep learning for early diagnosis and molecular subtyping of NSCLC, as illustrated in Figure 1. First, the SERS-active probe PACD was prepared with AuNCs adsorbed onto the surface of PS and the anti-CD-9 antibody modified through the reaction of amino and carboxyl bonds. PACD serves as the capture probe and simultaneously as the SERS-enhancing substrate for exosomes. For exosome characterization, exosomes from NSCLC cells and PACD probes were introduced into the chip, where probes efficiently captured exosomes in the mixing chamber, and subsequently PACD with captured exosomes were retained in the size-based trapping chamber for SERS signal readout. Finally, a deep learning model was employed to conduct the classification of collected SERS spectral data of exosomes from three different NSCLC cell lines and one normal cell line, which characterized the different molecular features of exosomes and successfully distinguished NSCLC subtypes, while providing interpretable molecular insights critical for medical decision-making. This study not only demonstrates the powerful potential of combining microfluidic-SERS technology with deep learning but also provides a rapid and reliable approach for the early detection and molecular subtyping of NSCLC.

EXPERIMENTAL SECTION

Materials and Reagents. $HAuCl_4 \cdot 3H_2O$ was purchased from Invitrogen Trading Co. (Shanghai, China). 1-(3-(Dimethylamino)-propyl)-3-ethylcarbodiimide (EDC) was purchased from Sigma-Aldrich Company (Shanghai, China). Ascorbic acid (AA), sodium borohydride ($NaBH_4$), and anhydrous ethanol (ethanol) were purchased from Sinopharm (Shanghai, China). Trypsin (EDTA), cetyltrimethylammonium bromide (CTAB), phosphate buffer (PBS),11-mercaptoundecanoic acid (MUA), *N*-hydroxysuccinimide (NHS), and exosome extraction reagent (ExoQuick TC) were purchased from MacKlin (Shanghai, China). Rabbit anti-CD-9 polyclonal antibody was purchased from KGI Biologicals (Jiangsu, China). DMEM complete medium, RPMI-1640 complete medium, and exosome fluorescent dye (PKH26) were purchased from Yanjiang Biotechnology Company (Shanghai, China). Polystyrene microspheres (13 μm) were purchased from Tianjin Beisler Chromatography Technology Development Center (Tianjin, China). R6G was purchased from Tianjin Guangfu Fine Chemical Research Institute (Tianjin, China). All reagents were of analytical grade, and deionized water (18.25 MΩ·cm) obtained from the Milli-Q water purification system was used in all experiments.

Instruments. The surface morphology and dimensions of the substrates were characterized using a JEM-2100F (JEOL, Japan) high-resolution transmission electron microscope (TEM) and an FEI Inspect F50 (USA) field emission scanning electron microscope (SEM). UV−vis absorbance spectra were recorded using an Evolution 350 UV−vis spectrophotometer (Thermo Scientific, China). The hydrodynamic size of the nanoparticles was measured using a Zetasizer (Malvern Instruments, UK). FTIR characterization of AuNC@PS and AuNC@PS@CD-9 was performed using a Fourier transform infrared spectrometer (Thermo Scientific, China). Fluorograms of immunoprobe-captured exosomes and microfluidic chip structures were obtained using a confocal microscope STED (Leica). The morphology, concentration, and particle size of exosomes were characterized using a Hitachi HT-7700 transmission electron microscope (TEM) and a Particle Metrix nanoparticle sizer (NTA). All SERS spectra were acquired using an in situ confocal Raman spectrometer (HORIBA XploRA Plus).

PDMS Microfluidic Chip Design and Fabrication. The PDMS chip was prepared using stencil lithography: first, a pattern was formed on a chromium plate using photolithography; subsequently, SU-8 photoresist was uniformly coated on the wafer, and after UV exposure, the wafer was developed several times in a developer solution until there was no precipitation. The wafer was then made into a positive mold by blowing it dry with nitrogen and drying it under vacuum. Next, the PDMS and curing agent were mixed at a 10:1 ratio, debubbled, and cast on the male mold, then cured at 75 °C for 3 h. After the cured PDMS substrate was ultrasonically cleaned, it was treated with oxygen plasma and bonded to the glass substrate, and finally placed in a drying oven for 30 min to complete the preparation.

Preparation of AuNCs. First, AuNCs were synthesized using a seed growth method.[30,31] Specifically, 250 μL of $HAuCl_4$ (0.01 M) solution was added to 7.5 mL of CTAB (0.1 M) solution, followed by the rapid addition of 0.6 mL of freshly prepared ice-cold $NaBH_4$ (0.01 M) solution. The mixture was stirred using a magnetic stirrer at 500 rpm for 2 min. The color of the mixed solution rapidly changed to light brown, and it was kept stirring for 2 min before being incubated in a water bath at 30 °C for 2 h to obtain the seed solution. Next, the growth solution was prepared by adding 3.2 mL of CTAB (0.1 M), 0.4 mL of $HAuCl_4$ (0.01 M), and 1.9 mL of AA solution (0.1 M) to 16 mL of deionized water. To initiate the growth of AuNCs, 12 μL of the 6-fold diluted seed solution was taken and added to the growth solution, followed by stirring with a magnetic stirrer at 500 rpm for 30 s. The solution was then incubated in a water bath at 30 °C for 2 h. Finally, AuNCs were obtained by centrifugation at 8000 rpm for 16 min and redispersed in deionized water.

Preparation of AuNC@PS Composites. The AuNC@PS composites were prepared primarily through the electrostatic adsorption effect between negatively charged PS microspheres and positively charged AuNCs.[32] First, 10 μL of 1% (w/v) PS microsphere solution was washed with MES buffer twice. After the supernatant was discarded, the PS microspheres were redispersed in 0.4 mL of deionized water. Then, 2 mL of the AuNCs solution was mixed with the PS solution. The mixture was shaken in a constant-temperature water bath oscillator at 180 rpm for 3 h to ensure that the AuNCs were fully adsorbed onto the surface of the PS. Finally, the AuNC@PS composites were obtained by centrifugation at 3500 rpm for 10 min and redispersed in deionized water.

Preparation of SERS Immunoprobe. First, 1 mL of MUA (1 mM) ethanol solution was added to 1 mL of AuNC@PS solution, and the mixture was reacted at room temperature for 1 h. The thiol terminals in MUA bonded to AuNCs due to the strong affinity between sulfur and gold, while leaving the carboxyl terminals free. Subsequently, a solution containing 250 μL of EDC (0.4 M, in MES buffer) and 250 μL of NHS (0.1 M, in MES buffer) was added, and the mixture was reacted for 2 h, which enabled the exposed carboxyl groups of MUA to bind with the amino groups of the anti-CD-9 antibody.[33] Herein, CD-9 was selected primarily due to its high expression level on the exosomal surface and its functional relevance to tumor progression. The mixed solution was then centrifuged at 4000 rpm for 10 min, and this process was repeated twice to remove excess EDC and NHS. Next, 5 μL of anti-CD-9 antibody (10 μg/mL) was added, and the mixture was continuously shaken at 180 rpm for 1 h at 30 °C. Finally, the solution was washed by centrifugation twice, and the precipitate was resuspended in PBS solution for subsequent experiments.

Cell Culture and Exosome Extraction. The human normal lung epithelial cell line BEAS-2B and human NSCLC cell lines, including NCI-H460, NCI-H226, and PC-9, were purchased from the Cell Bank of the Chinese Academy of Sciences (Shanghai, China). These cell lines were cultured in DMEM and RPMI-1640 complete media supplemented with 10% fetal bovine serum and 1% penicillin in 5% CO2 atm at 37 °C. After 70% confluence was reached, the cells were washed three times with 0.01 M PBS buffer. Subsequently, complete medium containing Exo-Free FBS was added, and the cells were further cultured for an additional 48 h. Five mL of cell supernatant was collected and centrifuged at 3000 × *g* for 15 min to remove cellular debris. 1 mL of ExoQuick TC reagent was added and mixed thoroughly by inverting and gently tapping. The mixture was incubated at 4 °C for 12 h, followed by centrifugation at 1500 × *g* for 30 min. After discarding the supernatant, it was centrifuged again

https://doi.org/10.1021/acssensors.4c03621
ACS Sens. 2025, 10, 2872−2882

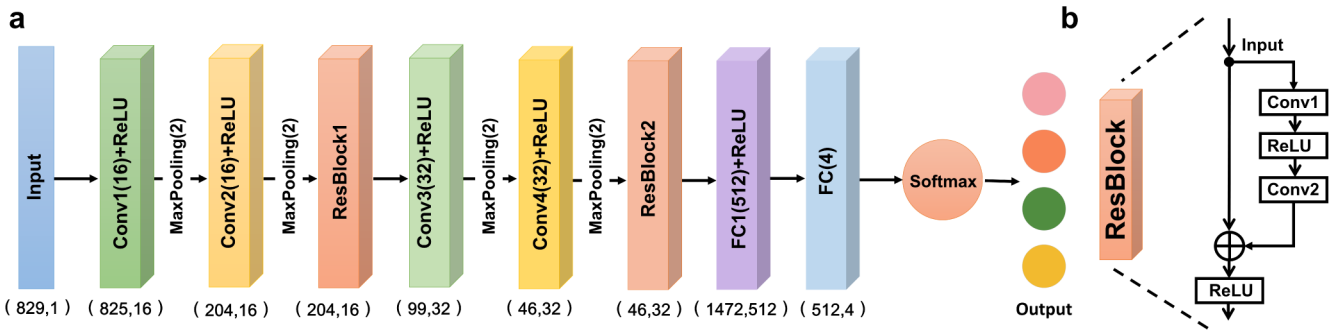

Figure 2. (a)Architecture of the deep learning model. (b) Architecture of the ResBlock.

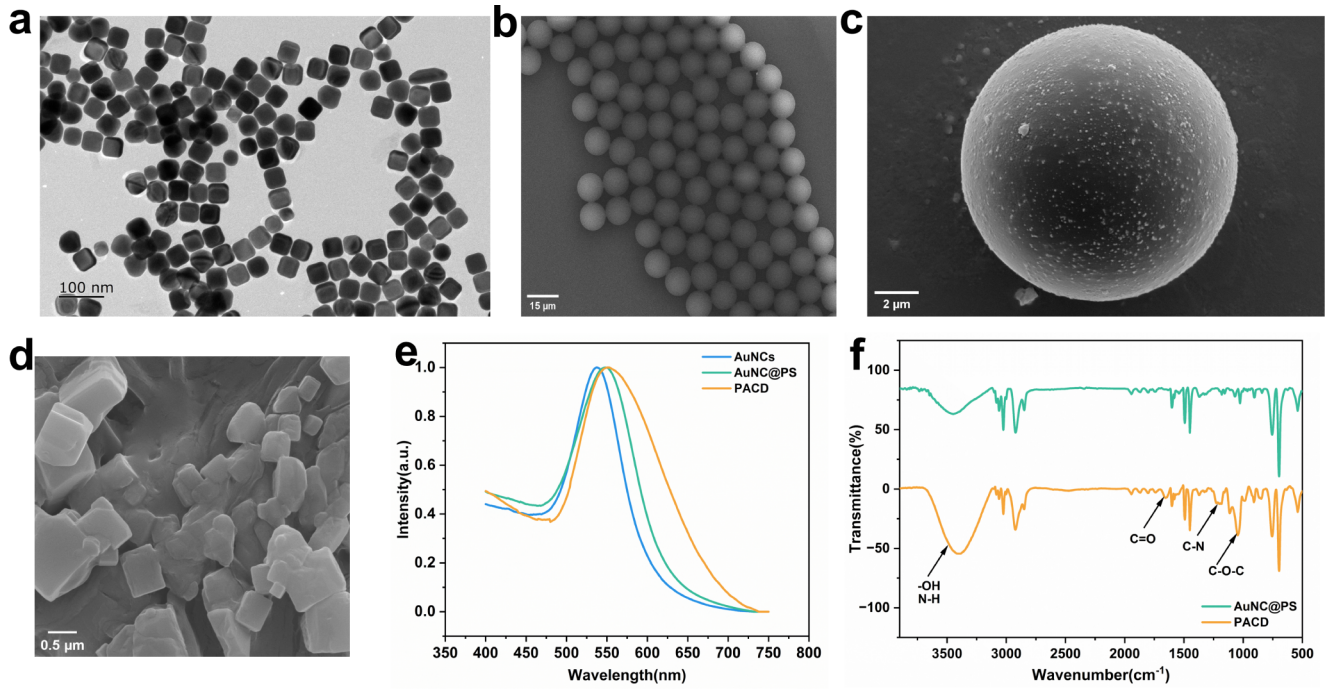

Figure 3. Characterization of SERS-active capture probes. (a) TEM image of AuNCs. (b) SEM image of PS. (c,d) SEM images of AuNC@PS at different magnifications. (e) Absorption spectra of AuNCs, AuNC@PS, and PACD. (f) FTIR spectra of AuNC@PS and the PACD.

at 1500 × *g* for 5 min. Finally, the collected exosomes were resuspended in 100 μL of PBS solution and stored at −80 °C for subsequent experiments.

Exosome Capture and SERS Detection in a Microfluidic Chip. All SERS spectra were acquired using a confocal Raman microscope. PACD solution and exosome solution were simultaneously introduced into the chip through inlets 1 and 2, respectively, at a flow rate of 16.5 mm/s for 2 min. The two solutions were mixed and reacted within the mixing chamber and were simultaneously transported to the trapping chamber. The PACD−exosome complexes were immobilized in the Raman detection area and incubated for 1 h. PBS buffer was continuously infused through inlet 3 at a rate of 10 mm/s for 1 min to wash away excess exosome solution and PACD from the mixing chamber. Exosomes were then detected using Raman spectroscopy. During the measurement process, excitation was performed using a 638 nm laser with a power of 3 mW and an integration time of 3 s. The spectral range was from 300 cm^{-1} to 1800 cm^{-1}, containing rich vibrational modes of proteins, lipids, carbohydrates, and nucleic acids. All spectra were collected under identical conditions. Prior to data analysis, a spectral baseline correction was performed using LabSpec6.

Data Preprocessing and Augmentation. The obtained raw SERS spectra were subjected to preprocessing to obtain a set of high-quality spectral data. Given that smoothing or scattering correction of SERS spectra may result in distorted features, only baseline correction was performed on the original spectra using the software LabSpec6. Subsequently, we further augmented the dataset by adding Gaussian white noise to the original signals, which contributes to enhancing robustness and mitigating overfitting. In this study, we added noise with signal-to-noise ratios (SNRs) of 10 and 30 dB to each of the original spectra, respectively. Thus, 944 collected SERS spectra were extended to a dataset of 2832 spectra, which was randomly shuffled and divided into a training set and a test set in a 7:3 ratio.

Construction of Deep Learning Model. The model was constructed using Python 3.9.12 and PyTorch 2.0.0, which was run in a CUDA 12.2 environment using a single NVIDIA GeForce RTX 4060 laptop GPU. As shown in Figure 2a, the network consists of an input layer, four convolutional layers, four pooling layers, two residual blocks, two fully connected layers, and an output layer. The spectral data ranged from 300 to 1800 cm^{-1} and consisted of 829 one-dimensional (1D) data points, which served as the input. The first two convolutional layers have a kernel size of 5, whereas the latter two layers have a kernel size of 7. Each convolutional layer is succeeded by a ReLU activation function to enhance the expressive power of the model. ResNet depends on shortcut connections, which directly transfer the input from a previous layer to the output of a subsequent layer, thereby preserving the gradient information from earlier layers and effectively resolving the vanishing gradient issues in deep networks. The residual blocks in the model, designated as ResBlock1

https://doi.org/10.1021/acssensors.4c03621
ACS Sens. 2025, 10, 2872−2882

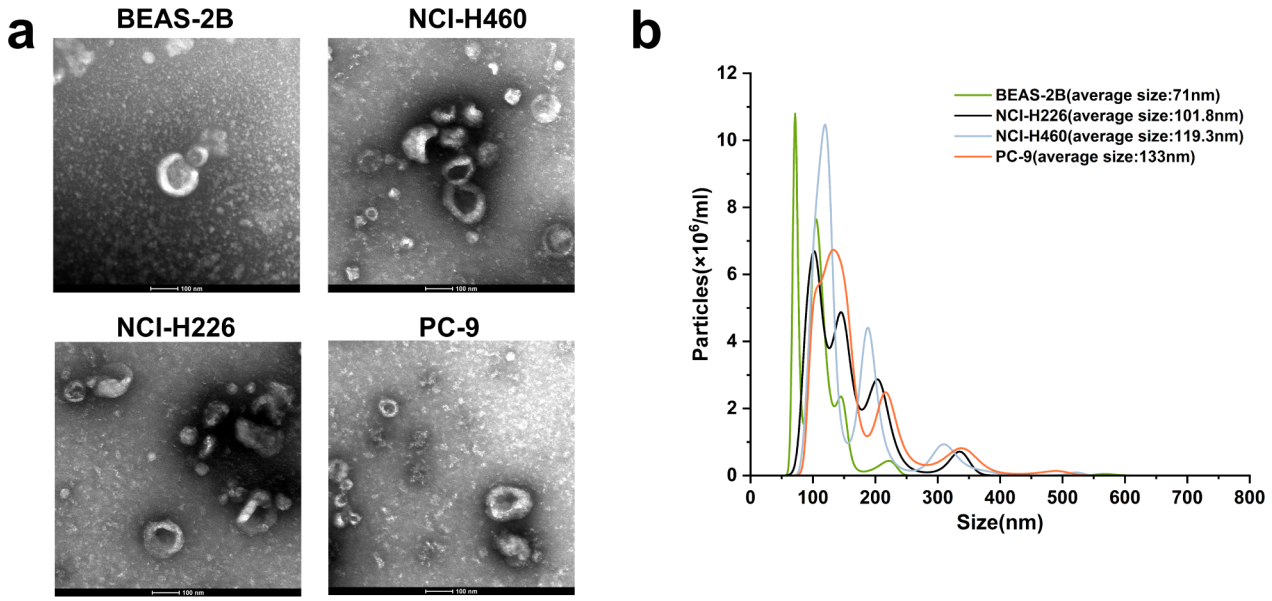

Figure 4. Characterization of exosomes. (a) TEM images of exosomes from BEAS-2B, NCI-H460, NCI-H226, and PC-9 cells. The scale bar: 100 nm (b) NTA of exosomes derived from various cell lines.

and ResBlock2, each comprise two convolutional layers with a kernel size of 3, as shown in Figure 2b. Finally, two fully connected layers and a Softmax function are utilized for classification. For the classification task of BEAS-2B, NCI-H460, NCI-H226, and PC-9, we assigned distinct labels (0, 1, 2, and 3) to each category. To accelerate convergence and improve model performance, the model adopted the Adam optimizer. The learning rate was set to 0.0001.

RESULTS AND DISCUSSION

Characterization of SERS-Active Capture Probes. First, AuNCs prepared by a seed-mediated method were adsorbed onto the surface of PS microspheres through electrostatic interaction to construct the AuNC@PS composites. As shown in Figure 3a, AuNCs characterized by TEM were observed to have a uniform cubic structure with a size of 70 nm. The SEM image in Figure 3b shows that PS microspheres are spherical and of uniform size, with a diameter of 13 μm. The PS microsphere in Figure 3c was observed to have a rough surface, which can be attributed to the conjugated AuNCs. This was further confirmed by the magnified SEM image in Figure 3d, showing the adsorbed AuNCs on the surface of PS. After characterizing their morphology, R6G was used as a Raman reporter to test the SERS performance of both AuNCs and AuNC@PS. The results (Figure S1) show that the SERS activity of AuNCs was maintained well after being adsorbed onto PS. As depicted in Figure 3e, AuNCs exhibited a localized surface plasmon resonance (LSPR) peak located at 538 nm.[34] After being conjugated with PS, the LSPR peak of AuNCs red-shifted to 548 nm, which can be attributed to the aggregated AuNCs and the increased refractive index of PS.[35] The anti-CD-9 antibody was then modified on the surface of AuNC@PS, resulting in a red-shifted LSPR absorption to 552 nm. The underlying reason for this is the formation of a protein corona around the AuNCs.[36] Dynamic light scattering (DLS) analysis, as shown in Figure S2, reveals that the zeta potential (ζ-potential) of AuNC@PS and PACD was 27.2 mV and −25.7 mV, respectively. This indicates that the solutions of AuNC@PS and PACD are relatively stable colloidal systems. FTIR spectroscopy was also employed to identify the anti-CD-9 antibody on the surface of AuNC@PS (Figure 3f). The broad band observed within the range of 3661−3127 cm^{-1} is mainly attributed to the stretching vibrations of the O−H and N−H bonds.[37] In the spectrum of PACD, the new band at 1665 cm^{-1} can be assigned to the C═O group in the amide I band,[38] while the band variations in the region from 1249 cm^{-1} to 1142 cm^{-1} correspond to the C−N stretch in the amide III band.[37] A more intense absorption band within the range of 1090 cm^{-1} to 1005 cm^{-1} was observed in PACD, which is attributed to the asymmetric stretching of the C−O−C bond.[39] These observations further confirm the successful conjugation of the antibody. Additionally, to visually determine whether the anti-CD-9 antibody had successfully bonded, fluorescence imaging was carried out. Exosomes were first stained with PKH26 and then incubated with capture probes PACD, while AuNC@PS incubated with stained exosomes was used as a control. As shown in Figure S3a, fluorescence signals overlapping with microspheres suggested that exosomes were captured by PACD. However, no fluorescence signals were observed in Figure S3b because the anti-CD-9 antibody was not conjugated. Then, we measured the SERS spectra of the pristine AuNC@PS, AuNC@PS-MUA-anti-CD-9 (before and after the capture of exosomes from NCI-H226 cells), which showed very different features (Figure S4). No obvious signals of pristine AuNC@PS could be observed. Compared to the AuNC@PS -MUA-anti-CD-9 , more pronounced and distinctive SERS bands emerged in the spectra of the AuNC@PS-MUA-anti-CD-9 with exosome sorption. While the MUA and anti-CD-9 antibody modification may moderately reduce direct exosome-AuNC surface contact, the proximity with a maximum distance of 7 nm from the metal surface (see Figure S5 for details) ensured exosomes reside within the effective LSPR enhancement region. All these results demonstrate the successful synthesis of SERS-active capture probes PACD.

Characterization of Exosomes. Cellular exosomes were isolated and purified using the ExoQuick-TC kit, which were then characterized by TEM and nanoparticle tracking analysis (NTA). Figure 4a reveals that all cell-derived exosomes display a typical cup-shaped morphology along with a distinct lipid

https://doi.org/10.1021/acssensors.4c03621
ACS Sens. 2025, 10, 2872−2882

bilayer structure. The NTA results in Figure 4b indicate that the size of the exosomes ranges from 30 to 150 nm, which falls within the typical range. These findings confirm that the exosomes were successfully isolated from the cell culture medium.

Working Principle and Characterization of the Microfluidic-SERS Chip. Figure 5 shows the schematic drawing of the integrated microfluidic-SERS chip and its working principle, which comprises three inlets, one outlet, one mixing chamber, and one trapping chamber. The chip was connected to a microinjection pump through tubing. First, PBS buffer was slowly and uniformly injected through all three inlets to rinse the interior of the chip. Afterward, 0.5 mL of exosome and SERS-active capture probe PACD solutions were respectively injected into the chip through inlets 1 and 2. Exosomes and capture probes entered the mixing chamber, where they could fully mix and react for the capture of exosomes. The mixed solution was then continuously transported to the trapping module of the chip, which enabled size-based trapping of PACD-exosome complexes. PS microspheres with a uniform diameter of 13 μm enabled efficient exosome trapping within the chip via a size-dependent array, leveraging their precise dimensions. The array was meticulously designed based on the specific size of the PS microspheres, creating a tailored spatial configuration for exosome capture. In the experiment, the capture probes and exosomes were continuously injected for 3 min to ensure thorough mixing. Subsequently, PBS buffer was continuously injected through inlet 3 for 1 min to wash away the excess reaction mixture within the chip. Finally, a confocal Raman spectrometer was used for SERS detection of exosomes in the trapping array.

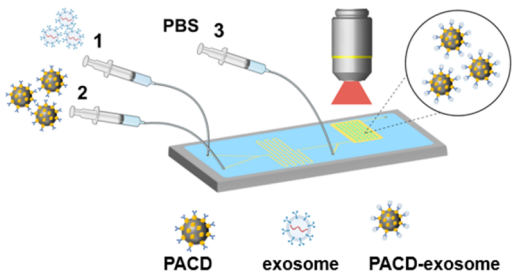

Figure 5. Sketch of the integrated microfluidic-SERS chip for exosome capture and detection.

The microfluidic-SERS chip designed for this study is presented in Figure 6a,b, featuring three inlets, one mixing chamber, one trapping chamber, and one outlet. The mixing chamber consists of continuous S-bends (Figure 6c), while the trapping chamber consists of rows of microarrays, each array being composed of two inclined capsule-shaped pillar structures (Figure 6d). The chip has a length of 25 mm, a width of 18 mm, and a thickness of 5 mm. Detailed data are provided in Figure S6a−d. When the liquid flowed through the S-shaped channel and reached the trapping chamber, the micropillar array also functioned as a mixer, increasing the chances of collisions and binding between exosomes and capture probes. Simulation of the flow rate and pressure field within the mixing chamber and the trapping chamber confirmed this continuous effect (Figure 6e,f). It indicated that the fluid was uniformly distributed within the S-shaped bends and the trapping chamber, and the pressure gradient was reasonable, ensuring effective mixing of exosomes with the capture probes. In addition, after red ink was injected into the

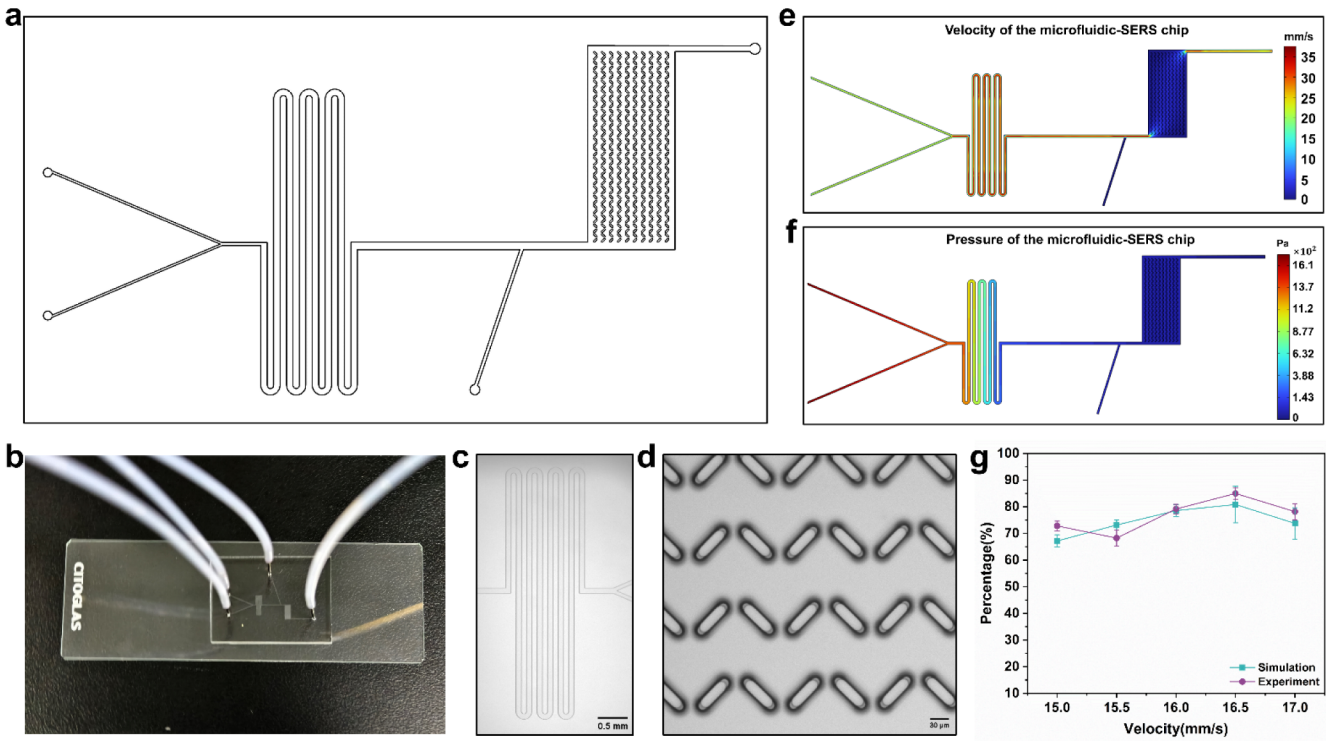

Figure 6. (a) CAD diagram of the microfluidic-SERS chip. (b) A prototype of the microfluidic-SERS chip. (c) Mixing chamber of the chip. (d) Trapping chamber of the chip. (e) Velocity distribution map of the microfluidic-SERS chip. (f) Pressure distribution map of the microfluidic-SERS chip. (g) Trapping efficiency of the chip.

https://doi.org/10.1021/acssensors.4c03621
ACS Sens. 2025, 10, 2872−2882

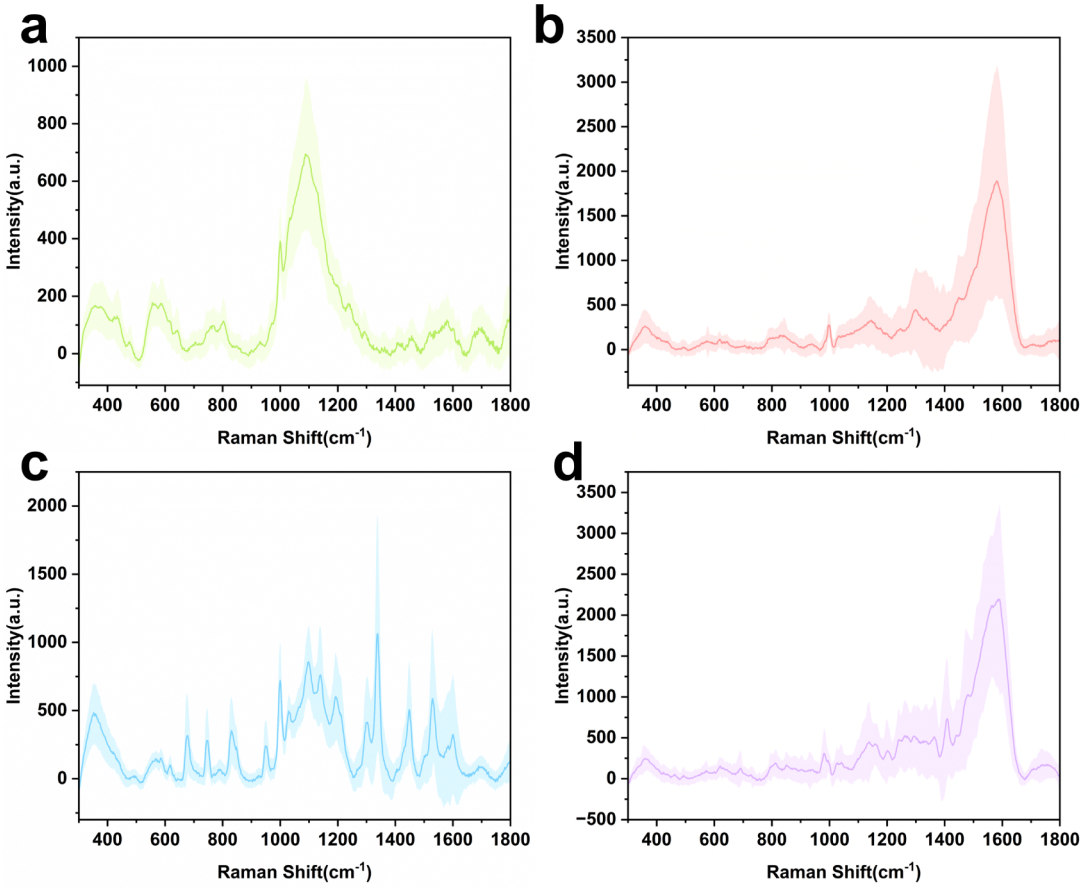

Figure 7. Average SERS spectra of exosomes from normal cells and different NSCLC cells. (a) BEAS-2B. (b) NCI-H460. (c) NCI-H226. (d) PC-9.

chip, no ink leakage was observed (Figure S6e), which indicated that the chip has excellent sealing properties.

To visually verify the exosome capture ability of PACD probes within the chip, PKH26-stained exosomes and the probes were introduced into the chip and allowed to react adequately. The chip was then subjected to fluorescence imaging. As shown in Figure S7, the fluorescence signals from exosomes overlapped with the probes, suggesting that exosomes were bonded with the probes. Meanwhile, exosome-bonded probes were trapped in inclined capsule-shaped pillars, which demonstrated that the PACD captured exosomes and the resulting PACD−exosome complexes were successfully trapped within the chip.

To validate the trapping efficiency of the chip, the trapping rate was calculated by determining the number of micropillar slots occupied by capture probes within the chip. Different flow rates were selected to test the capture efficiency. According to both simulation and experimental results (Figure 6g), with the increase in flow rate, the trapping efficiency rose to a maximum and then decreased. When the flow rate was set to 16.5 mm/s, the trapping efficiency reached a maximum of 85%. Therefore, the flow rate in subsequent experiments was set to 16.5 mm/s.

Exosomes Detection by the Microfluidic-SERS Chip. To validate the feasibility of the microfluidic-SERS chip for exosome detection, a confocal Raman spectrometer was used to collect the SERS spectra of exosomes derived from four different cell lines in the trapping array. During the experiment, we injected a mixed solution of exosomes and SERS-active capture probes into the chip at a rate of 16.5 mm/s for 2 min, followed by a 1-min rinse with buffer solution to ensure effective mixing, reaction, and capture. A notable highlight of this method is that it requires minimal sample consumption, and the entire detection process can be completed in an extremely short period of time. Ultimately, the capture probes effectively enhanced the Raman signal of the exosomes, allowing us to obtain clear spectral information. Figure 7a shows the average SERS spectrum of exosomes from normal human lung epithelial cells (BEAS-2B), serving as a control. Figure 7b−d displays the average SERS spectra of exosomes from three subtypes of NSCLC cells (NCI-H460, NCI-H226, and PC-9). These spectra exhibit distinct and sharp Raman vibration bands, including those at 356 cm^{-1}, 422 cm^{-1}, 538 cm^{-1}, 702 cm^{-1}, 784 cm^{-1}, 830 cm^{-1}, 997−1154 cm^{-1}, 1214 cm^{-1}−1302 cm^{-1}, 1362 cm^{-1}, 1378 cm^{-1}, 1480 cm^{-1}, 1526 cm^{-1}, 1585 cm^{-1}, 1602 cm^{-1}, and 1703 cm^{-1}, and 1712 cm^{-1}. These characteristic bands correspond to cellular proteins, nucleic acids, and lipids (Table S1 for details). From these characteristic features, different concentrations and compositions of exosomal molecules between normal and NSCLC cells were observed; however, these differences are subtle and complex. Consequently, if the cancer-specific characteristic patterns of exosomes can be discriminated between normal and lung cancer or among lung cancer subtypes, simultaneous diagnosis of multiple lung cancer subtypes would be possible.

To comprehensively evaluate the performance of the SERS-microfluidic chip, we systematically validated the reproducibility, limit of detection (LOD), and specificity of PACD for the SERS-microfluidic sensor. First, to assess chip reproducibility, we manufactured four batches of chips under identical

https://doi.org/10.1021/acssensors.4c03621
ACS Sens. 2025, 10, 2872−2882

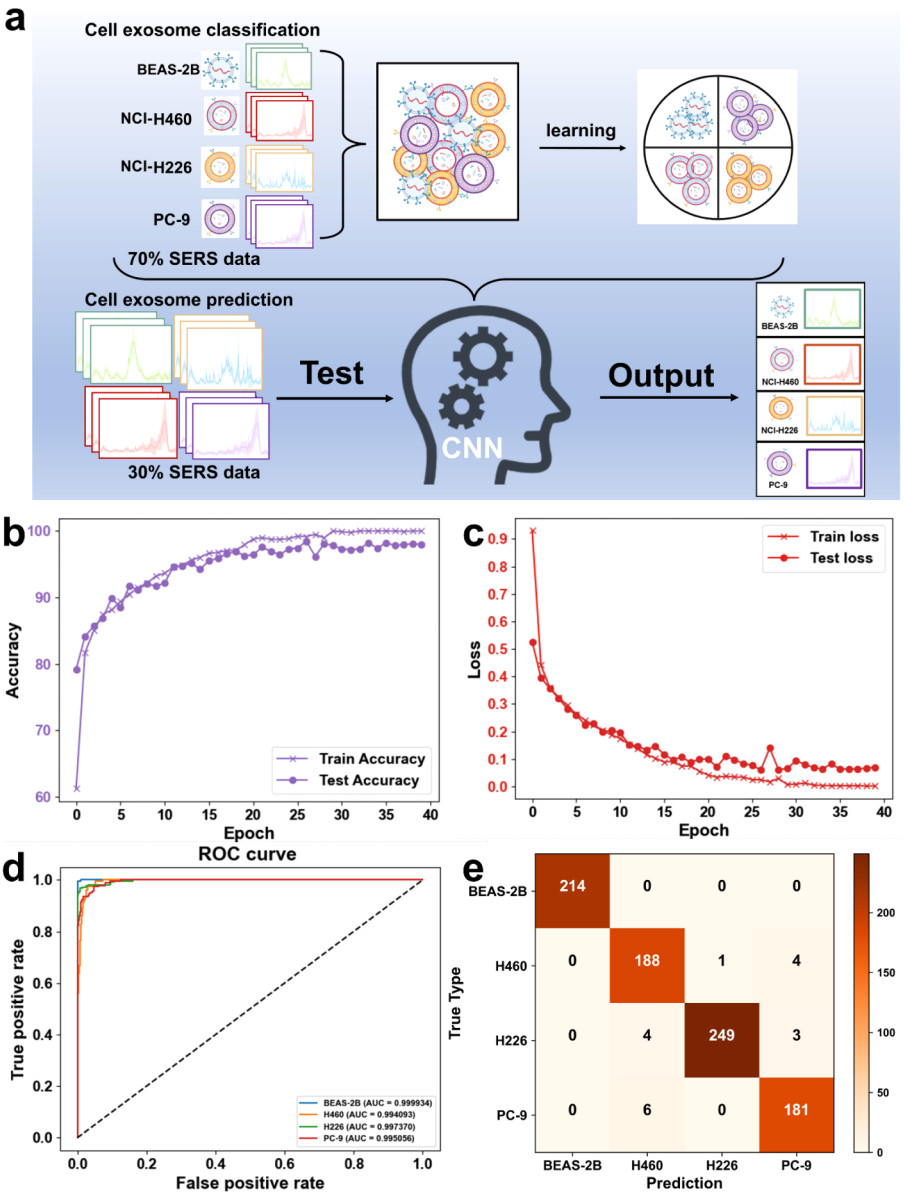

Figure 8. Deep learning-driven exosome classification. (a) Schematic illustration of deep learning-based cell exosome classification using exosomal SERS features. (b) Training and test accuracy curves. (c) Training and test loss curves. (d) ROC curves and their AUC values. (e) The confusion matrix.

conditions and collected the SERS spectra. The results showed that the average spectra from different chips highly overlapped, with consistent characteristic peaks (Figure S8). Meanwhile, to assess the reproducibility of SERS signals on the same chip, we randomly detected 10 SERS spectra from the trapping array on the same chip. No obvious differences were observed in characteristic band positions and band intensities (Figure S9), indicating that SERS detection within the same chip was also satisfactorily reproducible. The LOD values of the chip for exosomes from BEAS-2B, NCI-H460, NCI-H226, and PC-9 cells were tested to be 1.64×10^6, 2.66×10^5, 5.08×10^5, and 2.64×10^5 particles/mL, respectively, demonstrating the high sensitivity and robustness of the sensor (Figure S10). Finally, regarding PACD specificity, we conducted two sets of experiments in both PBS and 10% FBS environments, which demonstrated that there was no obvious nonspecific binding to PACD (Figure S11). Moreover, when AuNC@PS complexes were used as probes, no SERS signals were detected in the absence of the anti-CD9 antibody. These findings proved that PACD exhibits a high specificity for exosome detection (Figure S11). The experimental results collectively demonstrate that the developed SERS-microfluidic chip constitutes a promising platform for sensitive exosome analysis in complex biological matrices.

Deep Learning-enabled Discrimination of NSCLC Subtypes. To effectively discriminate among different cell lines and accurately diagnose NSCLC, label-free SERS characteristic patterns of cellular exosomes were analyzed using a deep learning algorithm (Figure 8a). A total of 944 SERS spectra were collected, including 245 from BEAS-2B exosomes, 219 from H460 exosomes, 254 from H226 exosomes, and 226 from PC-9 exosomes. To further enhance the generalization ability of the model, a data augmentation strategy was implemented, increasing the total number of SERS spectral datasets to 2832 entries. Subsequently, the dataset was scientifically divided into a training set and a test

https://doi.org/10.1021/acssensors.4c03621
ACS Sens. 2025, 10, 2872−2882

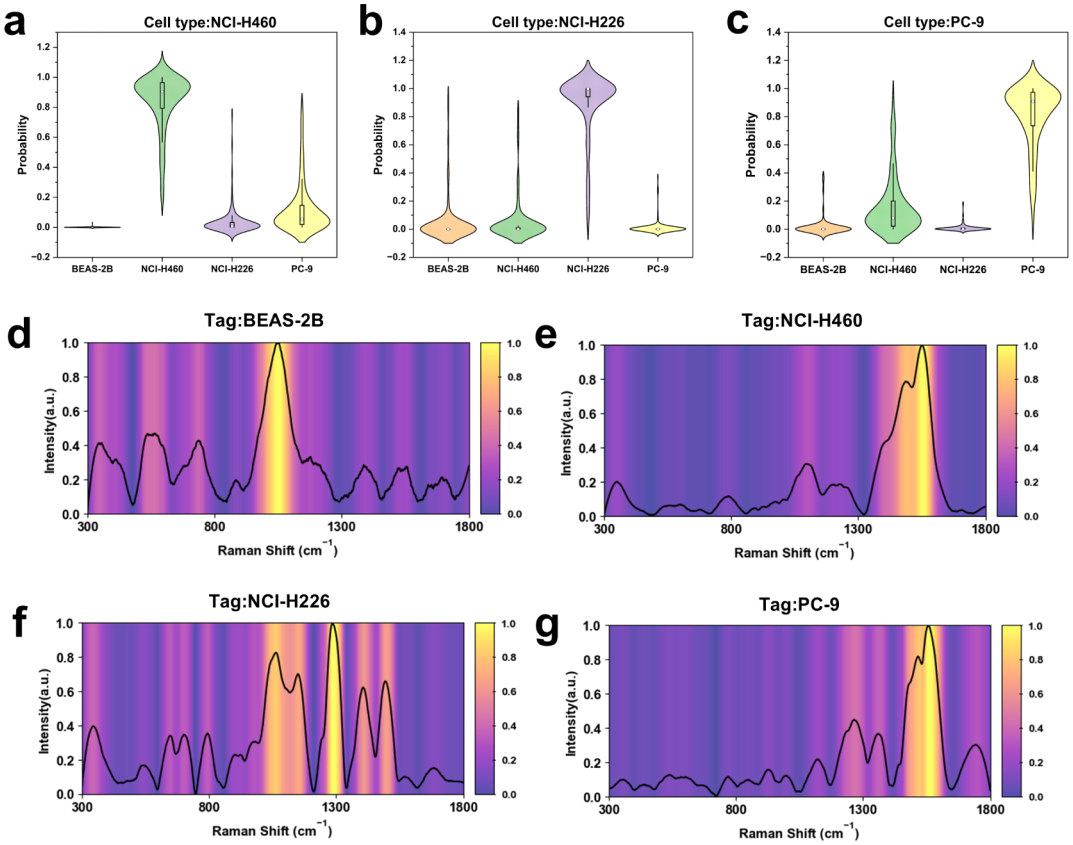

Figure 9. Output scores for NSCLC subtypes. (a) NCI-H460, (b) NCI-H226, and (c) PC-9. Visualizing the neural network was done by Grad-CAM. (d) BEAS-2B, (e) NCI-H460, (f) NCI-H226, and (g) PC-9.

set based on a 7:3 ratio to ensure adequate training of the model and verification of its performance.

During the training process, the variations in accuracy (ACC) and loss function (Loss) of the model were meticulously recorded, along with the results of the confusion matrix for the test dataset. Figure 8b,c clearly illustrate the trend of the evolution of the model's accuracy and loss function with learning iterations on both the training and test sets. After 40 epochs of training, the model achieved a classification accuracy of 97.88% on the test set, demonstrating excellent recognition capability. The value of the loss function decreased steadily and eventually stabilized. Meanwhile, given that only the training set was used for model training, the accuracy and loss changes of the test set with learning iterations were not significantly different from those of the training set, demonstrating that the optimized model was not overfitting. Figure 8d displays the confusion matrix of the optimized model for the test set. The confusion matrix visually reveals the number of correct and incorrect predictions for each category through its diagonal and off-diagonal numbers, providing detailed support for the model's performance. To further validate the accuracy of the model, as shown in Figure 8e, receiver operating characteristic (ROC) curves under the one-vs-rest classification were introduced, with the calculated area under the curve (AUC) values being 0.999, 0.994, 0.997, and 0.995, respectively. These results further indicate that the developed deep learning model has a high recognition capability for exosomes from different NSCLC subtypes.

Additionally, we employed the softmax activation function to normalize the prediction outputs and produced the corresponding label probability distribution plots. The softmax function can be calculated by eq 1, where K represents the number of labels, e^{z_i}, i is the exponent of the i-th element in the vector z, and $\sum_{j=1}^{K} e_j^z$ is the sum of the exponents of all elements in the vector z. As observed in Figure 9a–c, the exosomes from NSCLC subtypes, including NCI-H460, NCI-H226, and PC-9, exhibited higher scores within their respective categories, demonstrating the strong ability of the model to discriminate among different NSCLC subtypes based on SERS features of exosomes. Notably, the opaque decision-making process can undermine trust and utility. To intuitively elucidate the intrinsic mechanism of the model in processing SERS spectral data, gradient-based category activation mapping (Grad-CAM) was used for feature localization in SERS spectra, which visualized crucial features in the SERS spectra that contributed to lung cancer prediction and subtyping. This Grad-CAM-augmented explainable deep learning model provides substantial support for a better understanding of the decision-making process of the model and will potentially assist doctors in their assessments. Figure 9d–g shows the contribution of SERS characteristic bands to the classification. For normal cells, the main characteristic bands that contribute to classification are at 354 cm^{-1}, 669 cm^{-1}, 784 cm^{-1}, 1214 cm^{-1}, 1324 cm^{-1}, 1490 cm^{-1}, and 1541 cm^{-1}, while those for NSCLC cells are mainly concentrated at 356 cm^{-1}, 422 cm^{-1}, 702 cm^{-1}, 746 cm^{-1}, 803 cm^{-1}, 997 cm^{-1}, 1145 cm^{-1}, 1224 cm^{-1}, 1302 cm^{-1}, 1354 cm^{-1}, and 1589 cm^{-1}. These exosomes exhibit sharp Raman shift spectral peaks originating from proteins, nucleic acids, and lipids. Detailed information on the differential bands was listed in Table S1,

https://doi.org/10.1021/acssensors.4c03621
ACS Sens. 2025, 10, 2872−2882

which verified those bands contributing to NSCLC subtyping significantly (weighted value >0.75 in heatmap).

$$\text{softmax}(z) = \frac{e^{z_i}}{\sum_{j=1}^{K} e_j^z} \quad (1)$$

CONCLUSION

In this study, we have successfully developed a novel label-free SERS spectroscopy-integrated microfluidic platform in combination with deep learning for the efficient detection and classification of exosomes from NSCLC and normal lung epithelial cells. The platform exploits composites of AuNCs and PS microspheres functionalized with the anti-CD-9 antibody to form SERS-active capture probes for exosome capture and detection, achieving an outstanding capture rate of 85% within the microfluidic chip and subsequently offering SERS datasets of exosomes with high quality. The obtained exosomal SERS patterns were used to discriminate between different NSCLC subtypes by a deep learning model, which achieved a classification accuracy of 97.88% with an AUC of 0.99 for all categories. Concurrently, Grad-CAM highlighted interpretable molecular signatures in the spectral data to reflect the logical decision-making information behind the neural network. This study showcases the application of combining SERS-coupled microfluidics with deep learning in exosome-based liquid biopsy, featuring short analysis time, low sample consumption, highly sensitive detection, and powerful diagnostic functionality. The results may significantly improve the early diagnosis rate, precise subtyping, and personalized treatment outcomes for NSCLC.

ASSOCIATED CONTENT

Supporting Information

The Supporting Information is available free of charge at https://pubs.acs.org/doi/10.1021/acssensors.4c03621.

SERS performance, hydrodynamic size, zeta potential of AuNCs and AuNC@PS composites, functional validation of PACD probes, size estimation of the complex structure MUA-antibody CD9, geometric dimensioning of the chip, reproducibility, LOD, and specificity of the chip, characteristic Raman band assignments of exosomes (PDF)

AUTHOR INFORMATION

Corresponding Author

Hui Chen − *Key Laboratory of Optical Technology and Instrument for Medicine, Ministry of Education, University of Shanghai for Science and Technology, Shanghai 200093, China*; orcid.org/0000-0002-4391-9717; Email: chenhui@usst.edu.cn

Authors

Hongyi Liu − *Key Laboratory of Optical Technology and Instrument for Medicine, Ministry of Education, University of Shanghai for Science and Technology, Shanghai 200093, China*

Longqiang Xing − *Key Laboratory of Optical Technology and Instrument for Medicine, Ministry of Education, University of Shanghai for Science and Technology, Shanghai 200093, China*

Dandan Fan − *Key Laboratory of Optical Technology and Instrument for Medicine, Ministry of Education, University of Shanghai for Science and Technology, Shanghai 200093, China*

Nan Chen − *School of Electrical Engineering and Automation, Nantong University, Nantong 226019, China*

Pei Ma − *Key Laboratory of Optical Technology and Instrument for Medicine, Ministry of Education, University of Shanghai for Science and Technology, Shanghai 200093, China*

Xuedian Zhang − *Key Laboratory of Optical Technology and Instrument for Medicine, Ministry of Education, University of Shanghai for Science and Technology, Shanghai 200093, China*

Complete contact information is available at: https://pubs.acs.org/10.1021/acssensors.4c03621

Notes

The authors declare no competing financial interest.

ACKNOWLEDGMENTS

This work was supported by the National Natural Science Foundation of China (NSFC) (no. 62275156).

REFERENCES

(1) Cao, X.; Ge, S.; Zhou, X.; Mao, Y.; Sun, Y.; Lu, W.; Ran, M. A dual-signal amplification strategy based on pump-free SERS microfluidic chip for rapid and ultrasensitive detection of non-small cell lung cancer-related circulating tumour DNA in mice serum. *Biosens. Bioelectron.* **2022**, *205*, 114110.

(2) Li, M.-Y.; Liu, L.-Z.; Dong, M. Progress on pivotal role and application of exosome in lung cancer carcinogenesis, diagnosis, therapy and prognosis. *Mol. Cancer* **2021**, *20* (1), 22.

(3) Riely, G. J.; Wood, D. E.; Ettinger, D. S.; Aisner, D. L.; Akerley, W.; Bauman, J. R.; Bharat, A.; Bruno, D. S.; Chang, J. Y.; Chirieac, L. R.; DeCamp, M.; Desai, A. P.; Dilling, T. J.; Dowell, J.; Durm, G. A.; Gettinger, S.; Grotz, T. E.; Gubens, M. A.; Juloori, A.; Lackner, R. P.; Lanuti, M.; Lin, J.; Loo, B. W.; Lovly, C. M.; Maldonado, F.; Massarelli, E.; Morgensztern, D.; Mullikin, T. C.; Ng, T.; Owen, D.; Owen, D. H.; Patel, S. P.; Patil, T.; Polanco, P. M.; Riess, J.; Shapiro, T. A.; Singh, A. P.; Stevenson, J.; Tam, A.; Tanvetyanon, T.; Yanagawa, J.; Yang, S. C.; Yau, E.; Gregory, K. M.; Hang, L. Non-Small Cell Lung Cancer, Version 4.2024, NCCN Clinical Practice Guidelines in Oncology. *J. Natl. Compr. Cancer Network* **2024**, *22* (4), 249−274.

(4) Abdul Manap, A. S.; Ngwenya, F. M.; Kalai Selvan, M.; Arni, S.; Hassan, F. H.; Mohd Rudy, A. D.; Abdul Razak, N. N. Lung cancer cell-derived exosomes: progress on pivotal role and its application in diagnostic and therapeutic potential. *Front. Oncol.* **2024**, *14*, 1459178.

(5) Huang, K.; Yang, L.; Wang, Y.; Huang, L.; Zhou, X.; Zhang, W. Identification of non-small-cell lung cancer subtypes by unsupervised clustering of CT image features with distinct prognoses and gene pathway activities. *Biomed. Signal Process. Control* **2022**, *76*, 103643.

(6) Li, J.; Li, Y.; Chen, S.; Duan, W.; Kong, X.; Wang, Y.; Zhou, L.; Li, P.; Zhang, C.; Du, L.; et al. Highly Sensitive Exosome Detection for Early Diagnosis of Pancreatic Cancer Using Immunoassay Based on Hierarchical Surface-Enhanced Raman Scattering Substrate. *Small Methods* **2022**, *6* (6), 2200154.

(7) Lianidou, E.; Pantel, K. Liquid biopsies. *Genes, Chromosomes Cancer* **2019**, *58* (4), 219−232.

(8) Molina-Vila, M. A.; Mayo-de-Las-Casas, C.; Giménez-Capitán, A.; Jordana-Ariza, N.; Garzón, M.; Balada, A.; Villatoro, S.; Teixidó, C.; García-Peláez, B.; Aguado, C.; et al. Liquid Biopsy in Non-Small Cell Lung Cancer. *Front. Med.* **2016**, *3*, 69.

(9) Huang, L.; Rong, Y.; Tang, X.; Yi, K.; Wu, J.; Wang, F. Circular RNAs Are Promising Biomarkers in Liquid Biopsy for the Diagnosis of Non-small Cell Lung Cancer. *Front. Mol. Biosci.* **2021**, *8*, 625722.

(10) Tan, J.; Wen, Y.; Li, M. Emerging biosensing platforms for quantitative detection of exosomes as diagnostic biomarkers. *Coord. Chem. Rev.* **2021**, *446*, 214111.
(11) Cao, B.; Wang, P.; Gu, L.; Liu, J. Use of four genes in exosomes as biomarkers for the identification of lung adenocarcinoma and lung squamous cell carcinoma. *Oncol. Lett.* **2021**, *21* (4), 249.
(12) Song, F.; Wang, C.; Wang, C.; Wang, J.; Wu, Y.; Wang, Y.; Liu, H.; Zhang, Y.; Han, L. Multi-Phenotypic Exosome Secretion Profiling Microfluidic Platform for Exploring Single-Cell Heterogeneity. *Small Methods* **2022**, *6* (9), 2200717.
(13) Cao, X.; Mao, Y.; Gu, Y.; Ge, S.; Lu, W.; Gu, Y.; Li, Z. Highly sensitive and simultaneous detection of ctDNAs related to non-small cell lung cancer in serum using a catalytic hairpin assembly strategy in a SERS microfluidic chip. *J. Mater. Chem. B* **2022**, *10* (32), 6194−6206.
(14) Guo, L.; Shi, Y.; Liu, X.; Han, Z.; Zhao, Z.; Chen, Y.; Xie, W.; Li, X. Enhanced fluorescence detection of proteins using ZnO nanowires integrated inside microfluidic chips. *Biosens. Bioelectron.* **2018**, *99*, 368−374.
(15) Tang, X.; Tang, J.; Zhang, Q.; Suonanmu, D.; Zhang, Y.; Ren, Q.; Tao, F.; Li, C.; Wang, F. An integrated microfluidic cytosensor coupled with self-calibration electrochemical/colorimetric dual-signal output for sensitive and accurate detection of hepatoma cells. *Sens. Actuators, B* **2024**, *403*, 135176.
(16) Li, M.; Yang, P.; Wu, J.; Ni, R.; Yuan, H.; Guo, Z.; Zou, J.; Gao, W.; Cong, H.; Jin, Q. Highly efficient and label-free sensitive detection of tumor-derived exosome with an aptasensor-based microfluidic chip. *Microchem. J.* **2024**, *203*, 110875.
(17) Patra, B.; Sharma, M.; Hale, W.; Utz, M. Time-resolved non-invasive metabolomic monitoring of a single cancer spheroid by microfluidic NMR. *Sci. Rep.* **2021**, *11* (1), 53.
(18) Zhang, T.; Yang, Y.; Zhou, Y.; Lu, Y.; Zhang, M.; Liu, P.; Li, P.; Yang, L.; Li, Z. Microfluidic SERS chip for quantitative detection of weak surficial affinity molecules. *Appl. Surf. Sci.* **2024**, *654*, 159476.
(19) Li, L.; Zhang, L.; Gou, L.; Wei, S.; Hou, X.; Wu, L. Au Nanoparticles Decorated CoP Nanowire Array: A Highly Sensitive, Anticorrosive, and Recyclable Surface-Enhanced Raman Scattering Substrate. *Anal. Chem.* **2023**, *95* (29), 11037−11046.
(20) Qu, C.; Li, Y.; Du, S.; Geng, Y.; Su, M.; Liu, H. Raman spectroscopy for rapid fingerprint analysis of meat quality and security: Principles, progress and prospects. *Food Res. Int.* **2022**, *161*, 111805.
(21) Dey, S.; Vaidyanathan, R.; Reza, K. K.; Wang, J.; Wang, Y.; Nel, H. J.; Law, S.-C.; Tyler, J.; Rossjohn, J.; Reid, H. H.; Ibn Sina, A. A.; Thomas, R.; Trau, M. A microfluidic-SERSplatform for isolation and immuno-phenotyping of antigen specific T-cells. *Sens. Actuators, B* **2019**, *284*, 281−288.
(22) Zheng, X.-S.; Jahn, I. J.; Weber, K.; Cialla-May, D.; Popp, J. Label-free SERS in biological and biomedical applications: Recent progress, current challenges and opportunities. *Spectrochim. Acta, Part A* **2018**, *197*, 56−77.
(23) Pramanik, A.; Mayer, J.; Patibandla, S.; Gates, K.; Gao, Y.; Davis, D.; Seshadri, R.; Ray, P. C. Mixed-Dimensional Hetero-structure Material-Based SERS for Trace Level Identification of Breast Cancer-Derived Exosomes. *ACS Omega* **2020**, *5* (27), 16602−16611.
(24) Lee, Y.; Choi, K.; Kim, J.-E.; Cha, S.; Nam, J.-M. Integrating, Validating, and Expanding Information Space in Single-Molecule Surface-Enhanced Raman Spectroscopy for Biomolecules. *ACS Nano* **2024**, *18* (37), 25359−25371.
(25) Lyu, J.-W.; Zhang, X. D.; Tang, J.-W.; Zhao, Y.-H.; Liu, S.-L.; Zhao, Y.; Zhang, N.; Wang, D.; Ye, L.; Chen, X.-L.; et al. Rapid Prediction of Multidrug-Resistant Klebsiella pneumoniae through Deep Learning Analysis of SERS Spectra. *Microbiol. Spectrum.* **2023**, *11* (2), No. e04126-22.
(26) Xia, L.; Huang, Y.; Wang, Q.; Wang, X.; Wang, Y.; Wu, J.; Li, Y. Deciphering biomolecular complexities: the indispensable role of surface-enhanced Raman spectroscopy in modern bioanalytical research. *Analyst* **2024**, *149* (9), 2526−2541.
(27) Ye, Q.; Wu, M.; Xu, Q.; Zeng, S.; Jiang, T.; Xiong, W.; Fu, S.; Birowosuto, M. D.; Gu, C. Porous carbon film/WO3-x nanosheets based SERS substrate combined with deep learning technique for molecule detection. *Spectrochim. Acta, Part A* **2024**, *310*, 123962.
(28) Cao, D.; Lin, H.; Liu, Z.; Qiu, J.; Ge, S.; Hua, W.; Cao, X.; Qian, Y.; Xu, H.; Zhu, X. PCA-TLNN-based SERS analysis platform for label-free detection and identification of cisplatin-treated gastric cancer. *Sens. Actuators, B* **2023**, *375*, 132903.
(29) Chen, X.; Lin, K.; Chen, K.; Wang, L.; Liu, H.; Ma, P.; Zeng, L.; Zhang, X.; Sui, M.; Chen, H. Novel non-invasive method for urine mapping: Deep-learning-enabled SERS spectroscopy for the rapid differential detection of kidney allograft injury. *Spectrochim. Acta, Part A* **2024**, *315*, 124255.
(30) Wu, H.-L.; Kuo, C.-H.; Huang, M. H. Seed-Mediated Synthesis of Gold Nanocrystals with Systematic Shape Evolution from Cubic to Trisoctahedral and Rhombic Dodecahedral Structures. *Langmuir* **2010**, *26* (14), 12307−12313.
(31) Ziegler, C.; Eychmüller, A. Seeded Growth Synthesis of Uniform Gold Nanoparticles with Diameters of 15−300 nm. *J. Phys. Chem. C* **2011**, *115* (11), 4502−4506.
(32) Shi, Y.; Liu, Q.; Pan, Q.; Yang, D.; Lan, Y.; Wang, T. Adsorption of Cu Nanoparticles on Polystyrene-Based Microspheres. *Langmuir* **2024**, *40* (25), 13134−13143.
(33) Lee, C.; Carney, R.; Lam, K.; Chan, J. W. SERSanalysis of selectively captured exosomes using an integrin-specific peptide ligand. *J. Raman Spectrosc.* **2017**, *48* (12), 1771−1776.
(34) Ding, S.-J.; Zhu, J. Tuning the surface enhanced Raman scattering activity of gold nanocubes by silver coating. *Appl. Surf. Sci.* **2015**, *357*, 487−492.
(35) Dong, S.; Yi, L.; Cheng, L.; Li, S.; Yang, W.; Wang, Z.; Jiang, S. High-purity foam-like micron-sized gold cage material with tunable plasmon properties. *Sci. Rep.* **2020**, *10* (1), 16555.
(36) Majdinasab, M.; Azziz, A.; Liu, Q.; Mora-Sanz, V.; Briz, N.; Edely, M.; Lamy de la Chapellea, M. Label-free SERS for rapid identification of interleukin 6 based on intrinsic SERS fingerprint of antibody-gold nanoparticles conjugate. *Int. J. Biol. Macromol.* **2023**, *253*, 127560.
(37) Paul, D.; Roy, A.; Nandy, A.; Datta, B.; Borar, P.; Pal, S. K.; Senapati, D.; Rakshit, T. Identification of Biomarker Hyaluronan on Colon Cancer Extracellular Vesicles Using Correlative AFM and Spectroscopy. *J. Phys. Chem. Lett.* **2020**, *11* (14), 5569−5576.
(38) Gurbanov, R.; Bilgin, M.; Severcan, F. Restoring effect of selenium on the molecular content, structure and fluidity of diabetic rat kidney brush border cell membrane. *Biochim. Biophys. Acta, Biomembr.* **2016**, *1858* (4), 845−854.
(39) Hosseini, S.; Azari, P.; Jiménez-Moreno, M. F.; Rodriguez-Garcia, A.; Pingguan-Murphy, B.; Madou, M. J.; Martínez-Chapa, S. O. Polymethacrylate Coated Electrospun PHB Fibers as a Functionalized Platform for Bio-Diagnostics: Confirmation Analysis on the Presence of Immobilized IgG Antibodies against Dengue Virus. *Sensors* **2017**, *17* (10), 2292.

https://doi.org/10.1021/acssensors.4c03621
ACS Sens. 2025, 10, 2872−2882